Diffusion–deformation theory for amorphous silicon anodes: The role of plastic deformation on electrochemical performance

Citation: Di Leo, Claudio V. et al. "Diffusion–deformation Theory for Amorphous Silicon Anodes: The Role of Plastic Deformation on Electrochemical Performance." International Journal of Solids and Structures 67–68 (August 2015): 283–296 © 2015 Elsevier Ltd

As Published: http://dx.doi.org/10.1016/j.ijsolstr.2015.04.028

Publisher: Elsevier

Persistent URL: http://hdl.handle.net/1721.1/110969

Version: Author's final manuscript: final author's manuscript post peer review, without publisher's formatting or copy editing

Diffusion-deformation theory for amorphous silicon anodes: the role of plastic deformation on electrochemical performance

Claudio V. Di Leo, Elisha Rejovitzky, Lallit Anand*
Department of Mechanical Engineering
Massachusetts Institute of Technology
Cambridge, MA 02139, USA

April 13, 2015

Abstract

Amorphous Silicon (a-Si) is a promising material for anodes in Li-ion batteries due to its increased capacity relative to the current generation of graphite-based anode materials. However, the intercalation of lithium into a-Si induces very large elastic-plastic deformations, including volume changes of approximately 300%. We have formulated and numerically implemented a fully-coupled diffusion-deformation theory, which accounts for transient diffusion of lithium and accompanying large elastic-plastic deformations. The material parameters in the theory have been calibrated to experiments of galvanostatic cycling of a half-cell composed of an a-Si thin-film anode deposited on a quartz substrate, which have been reported in the literature. We show that our calibrated theory satisfactorily reproduces the mechanical response of such an anode — as measured by the changes in curvature of the substrate, as well as the electrochemical response — as measured by the voltage versus state-of-charge (SOC) response.

We have applied our numerical simulation capability to model galvanostatic charging of hollow a-Si nanotubes whose exterior walls have been oxidized to prevent outward expansion; such anodes have been recently experimentally-realized in the literature. We show that the results from our numerical simulations are in good agreement with the the experimentally-measured voltage versus SOC behavior at various charging rates (C-rates).

Through our simulations, we have identified two major effects of plasticity on the electrochemical performance of a-Si anodes:

- First, for a given voltage cut-off, plasticity enables lithiation of the anode to a higher SOC. This is because plastic flow reduces the stresses generated in the material, and thus reduces the potential required to lithiate the material.
- Second, plastic deformation accounts for a significant percentage of the energy dissipated during the cycling of the anode at low C-rates.

Hence, plasticity can have either (a) a beneficial effect, that is, a higher SOC for a given voltage cut-off; or (b) a detrimental effect, that is significant energy dissipation at low C-rates.

Keywords: A. Lithium-ion batteries B. Amorphous Silicon C. Diffusion D. Elasticity E. Plasticity

1 Introduction

The development of Li-ion batteries with improved capacity, life, safety, and cost, is of major importance for a wide range of industries — from large-scale stationary energy storage systems in renewable energy plants,

*Tel.: +1-617-253-1635; E-mail address: anand@mit.edu

to portable power systems for sustainable electric vehicles. In an attempt to increase capacity, researchers have proposed the use of lithium-metal alloys, e.g. lithium-silicon and lithium-tin alloys, or a combination of lithium-metal alloys and graphite, as potential anode materials since they possess a higher capacity for Li than the current-generation graphite anodes (cf., e.g., Hong et al., 1999; Tarascon and Armand, 2001; Scrosati and Garche, 2010). For example, when fully lithiated to $Li_{15}Si_4$, a silicon anode can theoretically achieve a specific capacity of $\sim 3.5\,\mathrm{Ah/g}$, which compares with only $0.37\,\mathrm{Ah/g}$ for the current-generation graphite anodes. However, the intercalation of such a large amount of Li into the silicon induces very large elastic-plastic deformations — with volume changes of approximately of $\sim 300\%$ (Obrovac and Krause, 2007). The two major mechanisms by which the large deformations of the anode negatively affect its performance are:

- *Fracture of the anode particles.* The large stresses that develop in the anode due to inhomogeneous volume changes associated with large gradients of Li-ions in the anode can lead to fracture of an anode particle. The formation and propagation of cracks in turn lead to degradation of the performance of the battery, and significantly limit its lifetime.

- *Failure of the solid electrolyte interface (SEI).* During operation of a Li-ion battery, a passivating film, known as the solid electrolyte interface (SEI), forms on the surface of the anode. Due to the large volumetric changes associated with the lithiation of Si anodes, the SEI is placed under large tensile stresses, which in turn cause it to fail. Repeated failure and growth of the SEI leads to capacity fade of the battery.

In order to develop a successful Si-based anode, both the problems mentioned above need to be addressed. Fracture of anode particles has been successfully mitigated through the use of nano- and micro-dimensioned particles. When the anode is composed of crystalline silicon (c-Si), nano-dimensioned materials have been successfully lithiated without fracture, even though lithiation in these materials occurs by a two-phase mechanism where pure c-Si reacts with Li, forming a heavily lithiated amorphous Li_xSi phase (often $Li_{15}Si_4$) behind a propagating phase front (cf., e.g., Ryu et al., 2011; Liu et al., 2012). More recently, it has been found that the lithiation behavior of *amorphous Si* (a-Si) is substantially different from that of c-Si. Indeed, a-Si nanoparticles have been observed to be quite robust to fracture during cycling (He et al., 2011; McDowell et al., 2012), and Berla et al. (2014) have recently shown that a-Si is resistant to fracture even at the micron scale ($\sim 2\mu$m). *In this paper, we focus on modeling the response of amorphous Silicon (a-Si) as an anode material.* For brevity, henceforth we often simply write Si rather than a-Si.

In order to mitigate failure of the SEI due to the large volume changes associated with lithiating Si anodes, various research groups have proposed the use of novel "engineered" anodes which restrict the deformation incurred by the SEI during cyclic lithiation. One such engineered anode, developed by Wu et al. (2012), consists of an ensemble of hollow Si nanotubes whose exterior surfaces have been oxidized to form silicon-dioxide. The electrolyte contacts the anode only at the silicon-dioxide surface, and thus the SEI grows only on the exterior of the nanotube and is not in contact with the Si. The relatively stiff silicon-dioxide shell acts as a mechanical constraint layer which prevents the outward expansion of the nanotube, and thus effectively restricts the deformation which is incurred by the SEI. However, the presence of the silicon-dioxide constraining layer leads to the generation of very large stresses during cyclic lithiation, forcing the Si anode to deform plastically towards the inside of the hollow nanotube. The elastic-plastic deformation of the Si anode, resulting from the mechanical constraint imposed by the silicon-dioxide layer, will have a significant effect on the electrochemical performance of the anode, which at present is largely unexplored, and is the focus of this paper. We expect, as noted by Sethuraman et al. (2010), that plasticity will play a role both in determining the energy dissipated during cycling of the anode as well as in determining the realizable capacity of the anode.

Recently, Zhao et al. (2011), Bower et al. (2011), and Anand (2012) have proposed theories which couple large elastic-plastic deformations with large volumetric swelling due to diffusion of lithium. Further, substantial progress has been made recently by Bucci et al. (2014) to calibrate the theory of Bower et al. (2011) to results from their experiments in which a half-cell based on an a-Si thin film deposited on a quartz substrate is electrochemically cycled while the curvature of the substrate is simultaneously measured; cf. also Pharr et al. (2014). However, to the best of our knowledge, such theories have not been used to determine how the elastic-plastic deformation of a-Si affects the electrochemical performance of anodes with

more complex geometries such as those of the oxidized hollow a-Si nanotubes of Wu et al. (2012).[1]

Accordingly, the purpose of this paper is to report on our theory and finite-element-based numerical simulation method for modeling geometrically complex a-Si anodes of the type studied by Wu et al. (2012). We have applied our simulation capability to quantifying how the elastic-plastic deformation deformation of engineered silicon anodes affects their electrochemical performance.

The paper is structured as follows. In Section 2 we summarize our theory for modeling a-Si anodes. In Section 3, in order to estimate the material parameters which are not directly available in the literature, we calibrate the material parameters of our theory to results from substrate curvature experiments available in the recent literature (Pharr et al., 2014; Bucci et al., 2014). In Section 4 we apply our fully calibrated theory to modeling the hollow double-walled Silicon nanotube anodes of Wu et al. (2012). Beyond comparing our simulation predictions to the results from their experiments, we investigate the importance of plasticity on the electrochemical behavior of such anodes. We finish in Section 5 with some final remarks.

2 Constitutive theory

Anand (2012) has formulated a general framework of balance laws and thermodynamically-consistent constitutive equations which couple Cahn-Hilliard-type species diffusion with large elastic-plastic deformations of a body, and accounts for the swelling and phase segregation caused by the diffusing species. In this paper we neglect any phase segregation mechanisms, and accordingly use a specialized form of Anand's theory which neglects a dependence of the free energy on the gradient of the species concentration.[2] Further, since our focus here is on modeling the response of a-Si, we limit our considerations to an isotropic theory. In order to model the experimentally-observed chemo-mechanical response of a-Si (e.g., Pharr et al., 2014; Bucci et al., 2014), the theory summarized below accounts for: (i) large elastic-plastic deformations using finite deformation kinematics; (ii) variation of the elastic moduli with varying lithium content; (iii) dependence of the yield strength on lithium content; and (iv) rate-sensitive plastic response.

Our theory relates the following basic fields:[3]

[1] We note that Zhao et al. (2012) have previously studied the generation of stresses in spherical and cylindrical hollow core-shell nanostructures. However, in their study they used various simplifying assumptions — e.g., rigid-perfectly-plastic material, no effect of concentration on the material properties, plane-strain conditions, uniform concentration, etc. Further, they made no attempt to model the voltage versus state-of-charge response of the system, and compare model predictions against experimental results.

[2] In their experiments McDowell et al. (2013) and Wang et al. (2013) have observed that a-Si nanoparticles appear to lithiate by a quasi-two-phase mechanism and not single-phase diffusional insertion of Li. The theory of Anand (2012) can be applied to modeling such two-phase lithiation mechanisms, cf. Di Leo et al. (2014). However, since such a quasi-two-phase mechanism appears to occur only *in the first half cycle* of lithiation, we do not account for such a mechanism in this paper.

[3] Notation: We use standard notation of modern continuum mechanics (Gurtin et al., 2010). Specifically: ∇ and Div denote the gradient and divergence with respect to the material point $\mathbf{X}$ in the reference configuration, and $\Delta = \mathrm{Div}\,\nabla$ denotes the referential Laplace operator; grad div, and div grad denote these operators with respect to the point $\mathbf{x} = \boldsymbol{\chi}(\mathbf{X}, t)$ in the deformed body; a superposed dot denotes the material time-derivative. Throughout, we write $\mathbf{F}^{e-1} = (\mathbf{F}^e)^{-1}$, $\mathbf{F}^{e-\top} = (\mathbf{F}^e)^{-\top}$, etc. We write $\mathrm{tr}\,\mathbf{A}$, $\mathrm{sym}\,\mathbf{A}$, $\mathrm{skw}\,\mathbf{A}$, $\mathbf{A}_0$, and $\mathrm{sym}_0\mathbf{A}$ respectively, for the trace, symmetric, skew, deviatoric, and symmetric-deviatoric parts of a tensor $\mathbf{A}$. Also, the inner product of tensors $\mathbf{A}$ and $\mathbf{B}$ is denoted by $\mathbf{A}:\mathbf{B}$, and the magnitude of $\mathbf{A}$ by $|\mathbf{A}| = \sqrt{\mathbf{A}:\mathbf{A}}$.

$\mathbf{x} = \boldsymbol{\chi}(\mathbf{X}, t)$	motion;
$\mathbf{F} = \nabla \boldsymbol{\chi}$	deformation gradient;
$\mathbf{F} = \mathbf{F}^e \mathbf{F}^p \mathbf{F}^s$	multiplicative decomposition of $\mathbf{F}$;
$\mathbf{F}^s, \mathbf{F}^p, \mathbf{F}^e$	swelling, plastic, and elastic distortions;
$\mathbf{F}^e = \mathbf{R}^e \mathbf{U}^e$	polar decompositions of $\mathbf{F}^e$;
$\mathbf{U}^e = \sum_{\alpha=1}^{3} \lambda_\alpha^e \mathbf{r}_\alpha^e \otimes \mathbf{r}_\alpha^e$	spectral decomposition of $\mathbf{U}^e$;
$\mathbf{E}^e = \sum_{\alpha=1}^{3} (\ln \lambda_\alpha^e) \mathbf{r}_\alpha^e \otimes \mathbf{r}_\alpha^e$	logarithmic elastic strain;
$\mathbf{E}_{\mathrm{H}}^e = \mathbf{R}^e \mathbf{E}^e \mathbf{R}^{e\top}$	spatial logarithmic elastic strain;
$\mathbf{T} = \mathbf{T}^\top$	Cauchy stress;
$\mathbf{M}^e = J^e \mathbf{R}^{e\top} \mathbf{T} \mathbf{R}^e$	Mandel stress;
c_{R}	molar concentration per unit reference volume;
$c_{\mathrm{R,max}}$	maximum molar concentration per unit reference volume;
$\bar{c} = c_{\mathrm{R}}/c_{\mathrm{R,max}} \in [0,1]$	normalized concentration;
$c = J^{-1} c_{\mathrm{R}}$	molar concentration per unit volume in the deformed body;
μ	chemical potential;
$\mathbf{j}$	spatial species flux vector.

2.1 Constitutive equations

1. **Kinematics.** Multiplicative decomposition of the deformation gradient,

$$\mathbf{F} = \mathbf{F}^e \mathbf{F}^p \mathbf{F}^s, \tag{2.1}$$

with

$$J = \det \mathbf{F} > 0, \qquad J^e = \det \mathbf{F}^e > 0, \qquad J^p = \det \mathbf{F}^p = 1, \qquad J^s = \det \mathbf{F}^s > 0. \tag{2.2}$$

2. **Swelling distortion.** Based on the isotropy of a-Si, we take the swelling distortion $\mathbf{F}^s$ to be spherical and to depend on the Li concentration,

$$\mathbf{F}^s = (J^s)^{1/3} \mathbf{1}, \quad \text{with} \quad J^s = 1 + \Omega(c_{\mathrm{R}} - c_{\mathrm{R}0}), \tag{2.3}$$

where Ω is a constant *partial molar volume* of the intercalating Li in the body, and $c_{\mathrm{R}0}$ is the initial concentration of Li.

3. **Free energy.** The free energy per unit reference volume is taken as

$$\psi_{\mathrm{R}} = \underbrace{\mu^0 c_{\mathrm{R}} + R\vartheta c_{\mathrm{R,max}} \Big(\bar{c} \ln \bar{c} + (1-\bar{c}) \ln(1-\bar{c}) + \sum_{n=2}^{7} a_n \cdot \bar{c}^{(n)} \Big)}_{\text{chemical energy}} + \underbrace{J^s \left(\frac{1}{2} \mathbf{E}^e : \mathbb{C}(\bar{c})[\mathbf{E}^e] \right)}_{\text{elastic energy}}. \tag{2.4}$$

Here, μ_0 is a reference chemical potential, R is the gas constant, ϑ is the absolute temperature, and the polynomial dependence $\sum_{n=2}^{7} a_n \cdot \bar{c}^{(n)}$ in the chemical free energy, in which a_n are fitting coefficients, is motivated by the recent paper Bucci et al. (2014). Further,

$$\mathbb{C}(\bar{c}) = 2G(\bar{c}) \mathbb{I} + (K(\bar{c}) - (2/3) G(\bar{c})) \mathbf{1} \otimes \mathbf{1}, \tag{2.5}$$

is a *concentration-dependent* elasticity tensor, with $G(\bar{c})$ and $K(\bar{c})$ concentration-dependent shear and bulk moduli, respectively.

4. **Stress.** The Mandel and Cauchy stress tensors are respectively given by,

$$\begin{aligned} \mathbf{M}^e &= J^{s-1} \frac{\partial \psi_{\mathrm{R}}}{\partial \mathbf{E}^e} = 2G(\bar{c}) \mathbf{E}^e + \left(K(\bar{c}) - \frac{2}{3} G(\bar{c}) \right) (\operatorname{tr} \mathbf{E}^e) \mathbf{1}, \qquad \text{and} \\ \mathbf{T} &= J^{e-1} \mathbf{R}^e \mathbf{M}^e \mathbf{R}^{e\top} = J^{e-1} \left(2G(\bar{c}) \mathbf{E}_{\mathrm{H}}^e + \left(K(\bar{c}) - \frac{2}{3} G(\bar{c}) \right) (\operatorname{tr} \mathbf{E}_{\mathrm{H}}^e) \mathbf{1} \right). \end{aligned} \tag{2.6}$$

5. **Chemical Potential.** The chemical potential of the Li in the anode is given by,

$$\begin{aligned}\mu &= \frac{\partial \psi_{\mathrm{R}}}{\partial c_{\mathrm{R}}} - \Omega \frac{1}{3}\mathrm{tr}\,\mathbf{M}^e \\ &= \mu^0 + R\vartheta \ln\left(\gamma \frac{\bar{c}}{1-\bar{c}}\right) - \Omega \frac{1}{3}\mathrm{tr}\,\mathbf{M}^e + \frac{J^s}{c_{\mathrm{R,max}}}\left(\frac{1}{2}\mathbf{E}^e : \frac{d\mathbb{C}(\bar{c})}{d\bar{c}}[\mathbf{E}^e]\right) + \Omega\left(\frac{1}{2}\mathbf{E}^e : \mathbb{C}(\bar{c})[\mathbf{E}^e]\right)\end{aligned} \tag{2.7}$$

where, following Bucci et al. (2014), we have defined an "activity coefficient" γ by

$$R\vartheta \ln(\gamma) = \sum_{n=2}^{7} a_n \cdot n \cdot \bar{c}^{(n-1)}. \tag{2.8}$$

The polynomial coefficients a_n are determined by fitting to experimental or numerical simulations of the open-circuit potential of Si during lithiation. Such a fit was performed by Bucci et al. (2014) for a-Si; we use their fitting coefficients in this paper.

6. **Evolution equation for $\mathbf{F}^p$.** The plastic distortion evolves according to

$$\dot{\mathbf{F}}^p = \mathbf{D}^p \mathbf{F}^p, \qquad \text{with} \qquad \mathbf{D}^p = \dot{\epsilon}^p \left(\frac{3\mathbf{M}_0^e}{2\bar{\sigma}}\right), \qquad \dot{\epsilon}^p \geq 0, \qquad \mathbf{F}^p(\mathbf{X}, 0) = \mathbf{1}, \tag{2.9}$$

where

$$\bar{\sigma} \stackrel{\text{def}}{=} \sqrt{3/2}|\mathbf{M}_0^e| \tag{2.10}$$

defines an *equivalent tensile stress*, and $\dot{\epsilon}^p$ denotes an *equivalent tensile plastic strain rate*. We introduce a positive-valued, stress-dimensioned, and concentration-dependent *yield strength* $Y(\bar{c}) > 0$, and assume that a no-flow condition,

$$\dot{\epsilon}^p = 0 \quad \text{if} \quad \bar{\sigma} \leq Y(\bar{c}), \tag{2.11}$$

holds. During plastic flow, $\dot{\epsilon}^p > 0$, the equivalent tensile stress is taken to be equal to a *rate-dependent flow strength*,

$$\bar{\sigma} = Y(\bar{c}) + Y_* \left(\frac{\dot{\epsilon}^p}{\dot{\epsilon}_0}\right)^{1/m}, \tag{2.12}$$

where $Y_* > 0$ is a positive-valued, stress-dimensioned constant, $\dot{\epsilon}_0$ is a reference tensile plastic strain rate, and m is a measure of the strain-rate sensititivy of the material. Equations (2.11) and (2.12) may be combined to give the equivalent tensile plastic strain rate as,

$$\dot{\epsilon}^p = \begin{cases} 0 & \text{if} \quad \bar{\sigma} \leq Y(\bar{c}), \\ \dot{\epsilon}_0 \left(\dfrac{\bar{\sigma} - Y(\bar{c})}{Y_*}\right)^m & \text{if} \quad \bar{\sigma} > Y(\bar{c}). \end{cases} \tag{2.13}$$

In order to model the experimentally-observed concentration-dependent change in the yield strength of a-Si, we adopt the following specific form for $Y(\bar{c})$,

$$Y(\bar{c}) = Y_{\mathrm{sat}} + (Y_0 - Y_{\mathrm{sat}}) \exp\left(-\frac{\bar{c}}{\bar{c}_*}\right), \tag{2.14}$$

with $\{Y_0, Y_{\mathrm{sat}}, \bar{c}_*\}$ three positive-valued material parameters. This function produces a simple exponential softening response from an initial value Y_0 to a lower saturation value $Y_{\mathrm{sat}} < Y_0$, with $\bar{c}_*$ controlling the rate of decay. Further, as a special value for Y_* in the rate-dependent response (2.12), we take

$$Y_* = Y_{\mathrm{sat}}. \tag{2.15}$$

7. **Species flux.** The *spatial flux* $\mathbf{j}$, of the intercalating Li is taken to depend on the *spatial gradient* $\mathrm{grad}\,\mu$, of the chemical potential:

$$\mathbf{j} = -m\,\mathrm{grad}\,\mu, \quad \text{with} \quad m = \frac{D_0}{R\vartheta} c(1-\bar{c}) \geq 0 \quad \text{the mobility.} \tag{2.16}$$

Here, D_0 is a constant diffusion coefficient.

Remark.

The constitutive equation (2.16) for the species flux differs from that in Anand (2012). In that paper it was the referential species flux, $\mathbf{j}_{\text{R}}$, which was taken to be given by a scalar mobility times the negative of the referential gradient of the chemical potential $(-\nabla\mu)$. We now believe that (2.16) is the more appropriate form for the species flux for large deformations of *continually isotropic materials*. Using standard transformation rules of continuum mechanics, the flux relation in the reference body corresponding to (2.16) is

$$\mathbf{j}_{\text{R}} = -\big(J\mathbf{C}^{-1}m\big)\,\nabla\mu, \qquad \text{with} \qquad \mathbf{C} = \mathbf{F}^{\top}\mathbf{F}.$$

□

2.2 Governing partial differential equations. Boundary and initial conditions

The governing partial differential equations consist of:

1. The local force balance
$$\text{div}\mathbf{T} + \mathbf{b} = \mathbf{0}, \tag{2.17}$$
where the Cauchy stress $\mathbf{T}$ is given by (2.6), and $\mathbf{b}$ is the non-inertial body force.

2. The local balance for the species concentration
$$\dot{c}_{\text{R}} = -J\,\text{div}\mathbf{j}, \tag{2.18}$$
with the flux $\mathbf{j}$ given by (2.16).

With $\mathcal{S}_{\mathbf{u}}$ and $\mathcal{S}_{\mathbf{t}}$ denoting complementary subsurfaces of the boundary $\partial\mathcal{B}_t$ of the deformed body $\mathcal{B}_t$, as boundary conditions we consider a pair of simple boundary conditions in which the displacement $\mathbf{u} = \mathbf{x} - \mathbf{X}$ is specified on $\mathcal{S}_{\mathbf{u}}$ and the surface traction on $\mathcal{S}_{\mathbf{t}}$:

$$\left.\begin{aligned} \mathbf{u} &= \breve{\mathbf{u}} \quad \text{on} \quad \mathcal{S}_{\mathbf{u}} \times (0,T), \\ \mathbf{T}\mathbf{n} &= \breve{\mathbf{t}} \quad \text{on} \quad \mathcal{S}_{\mathbf{t}} \times (0,T). \end{aligned}\right\} \tag{2.19}$$

With $\mathcal{S}_{\mu}$ and $\mathcal{S}_{\mathbf{j}}$ another pair of complementary subsurfaces of the boundary $\partial\mathcal{B}_t$, we also consider boundary conditions in which the chemical potential is specified on $\mathcal{S}_{\mu}$ and the spatial species flux on $\mathcal{S}_{\mathbf{j}}$

$$\left.\begin{aligned} \mu &= \breve{\mu} \quad \text{on } \mathcal{S}_{\mu} \times (0,T), \\ \mathbf{j}\cdot\mathbf{n} &= \breve{j} \quad \text{on } \mathcal{S}_{\mathbf{j}} \times (0,T). \end{aligned}\right\} \tag{2.20}$$

The initial data is taken as

$$\mathbf{u}(\mathbf{X},0) = \mathbf{0}, \quad \text{and} \quad \mu(\mathbf{X},0) = \mu_0(\mathbf{X}) \quad \text{in} \quad \text{B}. \tag{2.21}$$

The coupled set of equations (2.17) and (2.18), together with (2.19), (2.20) and (2.21) yield an initial/boundary-value problem for the displacement $\mathbf{u}(\mathbf{X},t)$ and the chemical potential $\mu(\mathbf{X},t)$

2.3 Electrolyte-anode interfacial reaction kinetics. Butler-Volmer equation

More details on our treatment of interfacial reaction kinetics may be found in Appendix A. As discussed in $(2.20)_2$, at a point on the surface of the deformed body we may prescribe a flux boundary condition, $\mathbf{j}\cdot\mathbf{n} = \breve{j}$. The prescribed flux $\breve{j}$ is related to an applied current per unit area by

$$I = -F\,\breve{j}, \tag{2.22}$$

where F is the Faraday constant. Conjugate to an applied flux at a point on the surface of the anode, there is a chemical potential, which we shall denote by μ^{surface}. The surface chemical potential μ^{surface} may be related to an electric potential by (c.f. A.16) through

$$U = V_0 - \frac{-\mu^{\text{surface}}}{F}, \tag{2.23}$$

where the potential U is commonly referred to as the *equilibrium potential*[4], and where V_0 is a reference potential which depends on the counter-electrode.

In order to model the electrochemical response of an anode, we must also account for the voltage drops at the anode/electrolyte interface due to out-of-equilibrium electrochemical reactions. With V the applied cell voltage, the driving force for the electrochemical reactions is given by (c.f. A.18)

$$\eta = V - U, \tag{2.24}$$

and is commonly referred to as the *overpotential*, since it is the potential above the equilibrium potential U required to drive Li into the anode. The current I per unit area (or equivalently the prescribed flux $\breve{j}$) is then presumed to be a function of the overpotential η, and is widely taken to be given by the phenomenological Butler-Volmer equation (cf., e.g., Newman and Thomas-Alyea, 2012; Bazant, 2013),

$$I = I_0\left(\exp\left(-\alpha\frac{F\eta}{R\vartheta}\right) - \exp\left(1-\alpha)\frac{F\eta}{R\vartheta}\right)\right), \tag{2.25}$$

where $0 < \alpha < 1$ is a symmetry factor which biases the reaction, and I_0 is a concentration-dependent exchange current, given by

$$I_0 = Fk_0(1-\bar{c})^{\alpha}\bar{c}^{(1-\alpha)}, \tag{2.26}$$

with the parameter k_0 a rate constant which is determined experimentally.

In our simulations we take $\alpha = 0.5$, in which case (2.25) may be inverted to yield

$$\eta = 2\frac{R\vartheta}{F}\sinh^{-1}\left(-\frac{1}{2}\frac{I}{I_0}\right), \quad \text{with} \quad I_0 = Fk_0(1-\bar{c})^{1/2}(\bar{c})^{1/2}. \tag{2.27}$$

Then, combining (2.27), (2.24), and (2.23), we may calculate the voltage V using the relation

$$V = V_0 - \frac{\mu^{\text{surface}}}{F} + 2\frac{R\vartheta}{F}\sinh^{-1}\left(-\frac{1}{2}\frac{I}{I_0}\right), \tag{2.28}$$

for an applied current I. We shall use this relation in our simulations to calculate the requisite voltage V for a prescribed current I.

2.4 Numerical implementation of the theory

We have implemented our coupled diffusion-deformation theory described in Sect. 2 by writing a user-element subroutine (UEL) for Abaqus/Standard (2010), for a 2D axisymmetric 4-node linear isoparametric quadrilateral element. Our numerical implementation is based on the procedures described in detail in the recent paper by Chester et al. (2014). Accordingly, for brevity, in this paper we omit all details of our numerical implementation.

[4]The electric potential U is an *equilibrium potential* in the sense that it relates to the interfacial voltage drop at the electrode/electrolyte interface when the electrochemical reactions at the interface are in equilibrium.

However, we note that in our numerical implementation we have ignored the last two terms in (2.7) for the chemical potential. These terms are quadratic in the elastic strains, and expected to be smaller in magnitude than the other terms in (2.7). Cf. Sethuraman et al. (2010) for arguments leading to such an approximation even for silicon, which can absorb a large amount of lithium, and for which the values of the elastic moduli are significantly affected when it is fully lithiated.

3 Calibration of the material parameters in the theory

The purpose of this section is to report on the calibration of the material parameters in our theory. The calibrated values are summarized in Table 1 at the end of this Section. A majority of the material properties necessary to characterize our constitutive theory are available in the literature. For the rest, we discuss in detail the procedures that we have used to estimate the values from published experimental data, primarily from the substrate-curvature experiments reported by Pharr et al. (2014).

3.1 Chemical properties

- The x in $\mathrm{Li}_x\mathrm{Si}$ represents the stoichiometric amount of Li in the compound $\mathrm{Li}_x\mathrm{Si}$. We assume here that Si may be fully lithiated to the compound $\mathrm{Li}_{15}\mathrm{Si}_4$, so that $x_{\max} = 3.75$. Note that x is related to the normalized concentration $\bar{c}$ by $x = x_{\max}\bar{c}$.
- With $\rho_{\mathrm{Si}} = 7.874 \cdot 10^4\,\mathrm{mol/m^3}$ the molar density of Si (Mohr et al., 2008), the maximum molar concentration of Li in Si is then given by $c_{\mathrm{R},\max} = 3.75 \cdot \rho_{\mathrm{Si}} = 0.295 \cdot 10^6\,\mathrm{mol/m^3}$.
- The maximum volumetric swelling of Si has been measured by Obrovac and Krause (2007) as $\Omega c_{\mathrm{R},\max} = 2.625$, and hence the partial molar volume of Li in Si is $\Omega = 8.89 \cdot 10^{-6}\,\mathrm{m^3/mol}$.
- The diffusivity D_0 of Li in Si has been measured by Ding et al. (2009) to be $D_0 = 10^{-16}\,\mathrm{m^2/sec}$.
- Finally, the coefficients used by Bucci et al. (2014) to fit the activity coefficient (2.8) are $a_2/F = 0.8735\,\mathrm{V}$, $a_3/F = 0.7185\,\mathrm{V}$, $a_4/F = -4.504\,\mathrm{V}$, $a_5/F = 6.876\,\mathrm{V}$, $a_6/F = -4.6272\,\mathrm{V}$, and $a_7/F = 1.1744\,\mathrm{V}$, where $F = 9.6485 \cdot 10^4\,\mathrm{C/mol}$ is the Faraday constant. The reference potential is $V_0 = 0.88\,\mathrm{V}$

3.2 Elastic properties

With

$$a = \frac{x}{x+1} = \frac{x_{\max}\bar{c}}{x_{\max}\bar{c}+1} \tag{3.1}$$

denoting the atomic fraction of Li atoms, the variation of the Young's modulus E, and the Poisson's ratio ν, with Li concentration is taken to obey a simple rule-of-mixtures proposed by Sethuraman et al. (2012),

$$E = a\,E_{\mathrm{Li}} + (1-a)\,E_{\mathrm{Si}}, \quad \text{and} \quad \nu = a\,\nu_{\mathrm{Li}} + (1-a)\,\nu_{\mathrm{Si}}, \tag{3.2}$$

where $(E_{\mathrm{Li}}, \nu_{\mathrm{Li}})$ are the elastic properties of pure Li, and $(E_{\mathrm{Si}}, \nu_{\mathrm{Si}})$ are the elastic properties of pure Si. Although the mixture rule (3.2) is linear with respect to the atom fraction a, see Fig. 1(a), it produces a non-linear result with respect to either the stoichiometric coefficient x or the normalized concentration $\bar{c} = x/x_{\max}$, as shown in Fig. 1(b). The elastic moduli (E, ν) are converted to (G, K) by using the standard relations $G = E/(2(1+\nu))$ and $K = E/(3(1-2\nu))$.

3.3 Plastic Properties. Reaction Constant

The remaining material properties that need to be calibrated are the plastic properties $\{Y_0, Y_{\mathrm{sat}}, \bar{c}_*, \dot{\epsilon}_0, m\}$ in equations (2.13) and (2.14), as well as the reaction constant k_0 in the expression $(2.27)_2$ for the exchange current I_0. Pharr et al. (2014) and Bucci et al. (2014) have recently reported on their novel experiments in which a half-cell based on an a-Si thin-film anode deposited on a quartz substrate is galvanostatically cycled against a Li electrode, while the curvature of the substrate is simultaneously monitored. We have calibrated the plastic properties and the reaction constant by conducting finite-element simulations of the substrate

curvature experiments and adjusting these material parameters so that pertinent numerical results match those which were measured experimentally by Pharr et al. (2014).

In the experiments of Pharr et al. (2014), a 100nm amorphous silicon film was deposited on a quartz substrate and first lithiated/delithiated galvanostatically against a Li-electrode in a half cell at a C-rate of 1/8 for one cycle. During the second cycle the lithiation rate was varied in order to induce different strain rates in the silicon film to probe the rate sensitivity of plastic flow of a-Si. During their experiment a substrate-curvature measuring technique was used to estimate the nominal stress in the a-Si film by using the classical Stoney formula (Stoney, 1909)

$$\sigma_n = \frac{1}{6}\frac{E_s}{1-\nu_s}\frac{h_s^2}{h_f}\kappa, \tag{3.3}$$

where κ is the experimentally-measured curvature of the substrate, E_s and ν_s are the Young's modulus and Poisson's ratio of the substrate, and h_s and h_f are the thicknesses of the substrate and the film layers, respectively.

As noted by Pharr et al. (2014), in their experiments there is loss of Li to the formation of SEI on the silicon anode. Thus, what is experimentally controlled during their galvanostatic experiments is the *total flux of lithium into the system*, j_{tot}, and not the flux of lithium, j_{Si} into the silicon anode; a portion j_{SEI} of the total flux in the system is consumed in the formation of the SEI. Thus,

$$j_{\text{Si}} = j_{\text{tot}} - j_{\text{SEI}}. \tag{3.4}$$

In our simulations we prescribe the flux of lithium into the silicon j_{Si}. Thus, in order to compare our simulations to the experimental results of Pharr et al. (2014), we need to estimate j_{SEI}. Following recent models of SEI formation (cf. e.g. Smith et al., 2011; Pinson and Bazant, 2013), and based on our previous paper on modeling SEI growth, Rejovitzky et al. (2014), we assume that the rate of loss of Lithium is inversely proportional to the square-root of time[5]

$$j_{\text{SEI}} = B/\sqrt{t}, \tag{3.5}$$

where B is a proportionality constant. Thus, combining (3.5) with (3.4), we obtain

$$j_{\text{Si}} = j_{\text{tot}} - B/\sqrt{t}. \tag{3.6}$$

The total flux j_{tot} depends on the charging rate and is determined by the experimental conditions. From the experiment results of Pharr et al. (2014) we have estimated that[6]

$$B = 1.3364 \cdot 10^{-5}\,\text{mol}/(\text{m}^2\text{sec}^{1/2}).$$

For later use we introduce the quantity

$$x_{\text{tot}} = \frac{A}{V}\frac{3.75}{c_{\text{R,max}}}\int_0^t j_{\text{tot}}\,d\tau, \tag{3.7}$$

which represents a normalized measure of the total amount of Li going into the system; here A and V are the initial area and volume of the a-Si anode respectively.

The simulation domain used to numerically represent the substrate curvature experiments of Pharr et al. (2014) is shown in Fig. 2. In order to minimize computational effort, we have only considered a small section of an axisymmetric plate adjacent to the axis of radial symmetry as the simulation domain, and meshed it with a single column of elements.[7] The silicon layer was meshed with 20 user-elements whose constitutive

[5]Bucci et al. (2014) have accounted for Li lost to SEI formation in a similar manner; however, they accounted for the flux of Li lost to SEI formation using a model which also depends on the applied voltage. Here, for simplicity, and since modeling SEI formation is not the main objective of this paper, we simply model loss of Li to SEI formation through (3.6).

[6]Specifically, from their voltage versus SOC plot, we estimate the difference in concentration at 1 V before and after the first cycle, and based on the experimental C-rate, determine how much Li was lost in one full cycle.

[7]In the experiments of Pharr et al. (2014), there is also a 15 nm layer of Ti and a 300 nm layer of Cu between the glass substrate and the silicon film. Since these layers are relatively stiff, and much thinner than the glass substrate, we do not include them in our finite element model.

behavior is described by the coupled diffusion-deformation theory summarized in Sect. 2. The glass layer is meshed with 20 built-in Abaqus elements whose constitute behavior is taken to be linear elastic with a Young's modulus of $E_s = 72\,\text{GPa}$ and Poissons ratio $\nu_s = 0.165$.

The boundary/initial conditions used for the substrate-curvature simulations are as follows:

- **Mechanical boundary conditions:** With respect to Fig. 2(b), consistent with radial symmetry, the nodes along edge AB are constrained to have zero radial displacement. All nodes along the edge CD are constrained to remain on a straight line as defined by the nodes at points C and D. The line formed by these nodes is free to move and rotate, and it is from the rotation of this line with respect to its initial vertical position that we compute the simulated curvature of the plate. Finally, the node at point B is constrained to have zero vertical displacement to prevent any rigid body motions.

- **Flux boundary conditions:** With respect to Fig. 2(b), on the nodes along edge AC we prescribe the flux of lithium according to (3.6). As in the experiment of Pharr et al. (2014), the total flux j_{tot} is set to correspond to a C-rate of 1/8 for the first full cycle. During the second cycle, the C-Rate was set to 1/8 for 1 h followed by a number of segments with different C-rates. The time of each segment was chosen such that the total flux into the system during each segment was equal. Specifically, C-rate jumps from 1/8 to
$$\text{C-rate} \in [1/2, 1/4, 1/16, 1/32, 1/64, 1/128], \tag{3.8}$$
were considered.

For an informative movie showing the results of such a simulation please see the supplementary movie S1_PlateCycling.mp4. This movie shows the time-dependent contour plots of the normalized concentration $\bar{c}$, the equivalent plastic strain $\bar{\epsilon}^p$, and the equivalent plastic strain rate $\dot{\bar{\epsilon}}^p$ on the deformed geometry of the a-Si. It also shows the variation of the nominal stress (cf. (3.3)) versus x_{tot} (cf. (3.7)), as well as the cell-voltage V (cf. (2.28)) versus x_{tot} during the experiment.

The results from our material parameter calibration procedure are shown in Figs. 3 and 4. Fig. 3(a) compares the simulated nominal stress (solid line) as a function of the total lithium content x_{tot}, against the corresponding experimental measurement (dashed line) (Pharr et al., 2014). The simulation captures the experimentally-observed behavior relatively well. In obtaining this fit the material parameters

$$\dot{\epsilon}_0 = 2.3 \cdot 10^{-3}\,1/\text{sec} \quad \text{and} \quad m = 2.94,$$

for the material rate-sensitivity were taken directly from Pharr et al. (2014), and only the the parameters

$$\{Y_0, Y_{\text{sat}}, \bar{c}_*\}$$

in (2.14) were adjusted to fit the data.

Fig. 3(b) shows the simulated voltage V (solid line) versus the total lithium content x_{tot}, against the corresponding experimental measurement (dashed line) (Pharr et al., 2014). Note that in the simulation shown in Fig. 3(b) we maintained a C-rate equal to 1/8; accordingly we have cropped the experimental data before the start of the C-rate jumps. The simulated voltage was computed using equation (2.28) by appropriately adjusting the parameter k_0 in the expression $(2.27)_2$ for the exchange current I_0. We adjusted k_0 so that the total dissipation of energy in one full cycle (i.e. the area inside the curves encompassed by the second and third half-cycles) in the simulation was approximately equal to that in the experiment.

With respect to the comparisons shown in Fig. 3, we make the following observations:

- In Fig. 3(a), the onset of plasticity, followed by plastic softening, occurs earlier in the simulation than in the experiment. This is likely due to the fact that we have *underestimated* the amount of Li lost to SEI formation in the early stages of lithiation.

- The functional form (2.14) for the variation of the yield strength with species concentration in the simulation captures the experimentally-observed plastic softening with increasing concentration, relatively well. During delithiation, the model as well as the experiments predict an increase in flow resistance due to a decrease in the concentration of lithium.

- The simulated elastic unloading after the first half-cycle matches well with the corresponding experimental results. This suggests that the mixing rule (3.2), combined with the elastic constants listed in Table 1, are well suited to characterizing the variation in elastic properties with changing Li concentration.

- As shown in Fig. 3(b), the simulation, using the reaction kinetics described in Sect. 2.3, gives a fairly good approximation of the experimentally-measured voltage versus x_{tot} response.

Finally, Figs. 4(b) and (c) compare the simulated and experimentally-measured stress-jumps due to changes in C-rate. Note that the axes in the two figures are identical in order to provide an accurate visual comparison of the stress increments and decrements with changes in C-rate. The simple power-law strain-rate-sensitivity for the a-Si in the theory produces stress-jumps which are comparable to those measured experimentally by Pharr et al. (2014).

The final list of calibrated values for a-Si is summarized in Table 1. Note that only the three material parameters $\{Y_0, Y_{\text{sat}}, \bar{c}_*\}$ for the rate-independent part of the plastic deformation resistance, and the reaction kinetics parameter k_0 for the exchange current have been fitted in this work; all the other parameters have been obtained from values published in the literature. With all the material parameters in the theory fixed to the values shown in this Table, in the next Section we apply our numerical simulation capability to model the hollow double-walled Silicon anodes developed by Wu et al. (2012).

Table 1: Material properties for our fully-coupled elastic-plastic deformation-diffusion model for amorphous Silicon anodes

	Parameter	Value	Source
Chemical	D_0	$10^{-16}\,\text{m}^2/\text{sec}$	Ding et al. (2009)
	$\Omega c_{\text{R,max}}$	2.625	Obrovac and Krause (2007)
	$c_{\text{R,max}} = 3.75 \cdot \rho_{\text{Si}}$	$0.295 \cdot 10^6\,\text{mol/m}^3$	$\rho_{\text{Si}} = 7.874 \cdot 10^4\,\text{mol/m}^3$ from Mohr et al. (2008)
	$[a_2, a_3, a_4, a_5, a_6, a_7]/F$	$[0.8735, 0.7185, -4.504, 6.876, -4.6272, 1.1744]\,\text{V}$	Bucci et al. (2014)
Elastic	$E_{\text{a-Si}}$	80 GPa	Sethuraman et al. (2012)
	$\nu_{\text{a-Si}}$	0.22	
	E_{Li}	4.91 GPa	
	ν_{Li}	0.36	
Plastic Rate-Dependent	$\dot{\epsilon}_0$	$2.3 \cdot 10^{-3}\,1/\text{sec}$	Pharr et al. (2014)
	m	2.94	
Plastic Rate-Independent	Y_0	1.6 GPa	Fitted to Pharr et al. (2014)
	Y_{sat}	0.4 GPa	
	$\bar{c}_*$	0.04	
Reaction Kinetics	k_0	$3.25 \cdot 10^{-7}\,\text{mol/sec}$	Fitted to Pharr et al. (2014)

4 Modeling a hollow double-walled a-Si nanotube anode

As discussed in the introduction, in order to mitigate failure of the SEI, various research groups have proposed the use of novel Si anode designs which restrict the deformation incurred by the SEI during cyclic lithiation. One such design, experimentally-realized by Wu et al. (2012), involves fabricating an anode which consists of an ensemble of hollow a-Si nanotubes whose outside has been oxidized; see Fig. 5(a) for a TEM image. These structures are referred by the authors as double-walled nanotubes, where the two walls refer to an interior Si core and an exterior silicon-dioxide shell; see schematic Fig. 5(b). Since the electrolyte contacts the anode only on its exterior surface — the exposed surface of silicon-dioxide, the SEI will also grow only on the exterior of the nanotube. During cycling, the relatively stiff silicon-dioxide shell acts as a mechanical constraint layer which prevents the outward expansion of the nanotube, effectively restricting the deformation incurred by the SEI.

In this Section we apply our calibrated fully-coupled theory for a-Si to model such a geometrically-complex anode design. We do so with *all material properties for a-Si fixed at the values shown in Table 1, which were calibrated from independent experiments*. In our simulations, the mechanical properties of the SiO_2 layer are simply taken to be linear elastic with a Young's modulus of $E = 90\,\text{GPa}$, and a Poisson's ratio of $\nu = 0.17$.

In modeling the hollow nanotubes of Wu et al. (2012), we assume that they are axisymmetric and have a length much larger than their diameter, so that diffusion of Li occurs entirely in the radial direction. In accordance with these assumptions, and in order to save computational effort, we take a sliver of the hollow tube, cf. Fig. 5(b), as our simulation domain, and mesh it with a single row of elements; cf. Fig. 5(c). With respect to Fig. 5(c) we apply the following boundary:

- **Mechanical boundary conditions:** The nodes along the edge AC are constrained to have zero-displacement in the vertical z-direction. Consistent with our assumption of a long thin tube, the nodes along edge DF are constrained to remain flat but are allowed to displace in the z-direction. The edges AF and CD are traction-free.

- **Chemical potential boundary conditions:** Consistent with our assumption of radial diffusion only, we constrain the chemical potential of the nodes on edge AC to equal the chemical potential of the nodes on edge DF.

- **Flux boundary conditions:** In these simulations we neglect the transport of Li through the SiO_2 layer. Then, consistent with the experiments which were done at a constant current, we prescribe a flux of Li into the Si directly on the nodes on edge BE. The magnitude of the flux is computed based on a desired C-rate through
$$\breve{j} = -(V/A)(\text{C-rate}/3600)c_{\text{R,max}},$$
where V and A are the initial volume and area of the Si anode respectively, and $c_{\text{R,max}}$ is the maximum molar concentration given in Table 1. In these simulations, for simplicity, we do not consider any loss of Li to SEI formation. As in the experiments of Wu et al. (2012), the simulated anode is cycled between voltage limits of 0.01 V and 1 V, where the simulated voltage is computed during the simulation using (2.28).

For later use, we define the state-of-charge (SOC) of the a-Si anode at a given time by

$$\text{SOC} = \int_{\text{B}} \bar{c}\, dV / \int_{B} dV. \tag{4.1}$$

Remark. As reported by Wu et al. (2012), and recently studied in detail by Zhang et al. (2014), it is expected that during cycling the SiO_2 film will react with Li to form a silicon-oxygen-lithium compound. This reaction, which is believed to be non-reversible, will consume lithium and also lead to an expansion of the SiO_2 film. In our simulations we do not attempt to model the uptake of Li, and the consequent expansion of the SiO_2 film during cycling. We make this purposeful choice for two reasons: (i) We would like to maintain our focus on the theory for a-Si and its response in the geometrically-complex anode under study; and (ii) It is unclear at present what the product of the reaction involving SiO_2 and Li is; and as

such, attempting to model this would result in a number of additional fitting parameters which cannot — at this stage of available experimental data — be independently determined. □

4.1 Typical simulation output

A typical result of our simulations is shown in Fig. 6, where we cycled a hollow double-walled nanotube anode at a C-rate of 1 for three half-cycles between voltage limits of 0.01 and 1V. On the left in Fig. 6 we show contours of the normalized concentration $\bar{c}$ (top), and contours of equivalent plastic strain $\bar{\epsilon}^p$ (bottom) in the a-Si. These contours are plotted at states (A) and (B), which respectively represent the states at the beginning and end of *the last half-cycle*; see the figure on the right, where these states are marked by dashed lines. From the contours of equivalent plastic strain we note that at the end of 3 half-cycles, the anode has accumulated a very large amount of plastic deformation — up to 210% plastic strain.

On the right of Fig. 6 we show plots of the equilibrium U (blue), and the voltage V (red), both as functions of the SOC. The difference between these two curves is the overpotential, $\eta = V - U$, which arises entirely due to the surface reaction kinetics described in Sect. 2.3. The equilibrium potential represents the intrinsic response of the Si anode, and visualizing it together with the voltage allows us to discern the contribution from the mechanical deformation of the Si anode to the overall voltage versus SOC behavior. The dissipation due to plastic deformation is evident in the hysteretic behavior of the equilibrium potential versus SOC curve. In this particular simulation, *plasticity accounts for* $\approx 15\%$ *of the total dissipation during one cycle.* For an informative animation of this cyclic simulation please see the supplementary movie "S2_HollowTube.mp4".

4.2 Comparison between our simulation results and the experiments of Wu et al. (2012)

Next, we compare our simulation results to the experimentally-measured voltage versus capacity curves of Wu et al. (2012). To convert the capacity data reported by these authors to SOC, we assume, as reported by the authors, that Si comprises 60% of the total mass of the active material, and that the maximum capacity of Si is 3.579 Ah/g. In order to compare the results from our simulations to those obtained experimentally, we ignore the results from the first half-cycle in our simulations, and shift the minimum SOC achieved in subsequent cycles to be zero. Fig. 7 (a) compares our simulated results (solid lines) for voltage versus SOC, against the experimental results (dashed lines) of Wu et al. (2012) at two C-rates — a C-rate of 1 (red) and a C-rate of 20 (blue). Although there are some discrepancies between the simulated and experimental results, our theory is capable of qualitatively reproducing the overall experimentally-measured response reasonably well.[8]

In order to get a more quantitative comparison between simulations and experiments, we may calculate two additional quantities from the voltage versus SOC curves at different C-rates:

- First, the *total dissipation* in one full cycle at a given C-rate is given by the corresponding area inside the voltage versus SOC curve.
- Second, the *maximum capacity* at a given C-rate corresponds to the capacity when the voltage hits the lower cutoff limit of 0.01 V.

We have carried out such calculations for several different C-rates. Fig. 7(b) shows the total dissipation as a function of C-rate — the simulations are shown as red circles, and the corresponding experiments are shown as black squares; note that the abscissa for the C-rates is logarithmic. It is clear from Fig. 7(b) that our simulations overestimate the total dissipation; however, our simulations correctly predict the experimentally-observed trend that the total dissipation is the largest at a C-rate ≈ 1, and decreases as the C-rate increases. The maximum capacity as a function of C-rate is shown in Fig. 7(c) — again the simulations are shown as red circles, and the corresponding experiments are shown as black squares. We obtain a good *quantitative prediction* of the experimentally-measured maximum capacity as a function of C-rate.

[8] In our simulations we have considered only a single nanotube, while the experimental results of Wu et al. (2012) were obtained from an anode which was made up of an *ensemble* of nanotubes of various dimensions. Some of the differences between the simulated and experimental results shown in Fig. 7 are clearly due to thme fact that we are considering only a single nanotube. In future work we aim to simulate an anode composed of many nanotubes of various dimensions.

We emphasize again that the results shown in Fig. 7 were obtained by using material properties for a-Si which were were calbrated from *independent experiments*. This shows that the theory and simulation capability presented in this paper is capable, with reasonable accuracy, of modeling the electrochemical response of a geometrically-complex Si anode.

4.3 Role of plastic deformation on the electrochemical response of the a-Si anode

The simulation capability developed here allows us to explore the role of plastic deformation on the voltage versus SOC behavior of the anode during cycling. We expect, as noted by Sethuraman et al. (2010), that plasticity will play a role both in determining the energy dissipated during cycling of the anode as well as in determining the realizable capacity of the anode.

First, we estimate the contribution of plasticity to the overall dissipation during cyclic lithiation/delithiation. Fig. 8(a) shows the plastic dissipation per cycle as a function of the C-rate. The dissipation due to plasticity is larger at low C-rates than at high C-rates. There are two factors that contribute to this behavior: First, since the plastic response of a-Si is rate-dependent, it exhibits a lower flow resistance at lower C-rates. Second, at low C-rates the voltage cutoff of 0.01 V is reached at higher values of SOC, and therefore the anode is deformed to a greater extent than at high C-rates.

Fig. 8 (b) shows the plastic dissipation normalized by the total dissipation (in percent) as a function of the C-rate. This figure clearly shows that at low C-rates plasticity plays a major role in the total dissipation of the anode over one cycle; *it accounts for over 30% of the total dissipation at a C-rate of 1/10.*

Although plasticity can contribute significantly to the total dissipation of energy of the anode per cycle, it also has the beneficial effect of relieving the build-up of elastic stresses in the material. This in turn reduces the voltage required to lithiate the anode to a particular SOC.

To illustrate this important effect we have performed simulations *suppressing plastic deformation*, while maintaining all other parameters constant. The results are shown in Fig. 9, where we compare a simulation with plasticity (red lines) to a simulation without plasticity (blue lines), both at a C-rate of 1. Fig. 9(a) compares the voltage V versus SOC for the two simulations. This figure clearly shows that the simulation without plasticity reaches the cutoff voltage of 0.01 V at a SOC of ≈ 0.3, whereas the simulation with plasticity reaches the cutoff at a much higher SOC of ≈ 0.7. The point in the first half-cycle where the two curves deviate indicates the onset of plasticity in the simulations with plasticity. Fig. 9(b) compares the equilibrium potential U versus SOC from the two simulations. Note that there is no discernible hysteretic behavior in the simulation without plasticity, since there is almost no dissipation of energy in the intrinsic behavior of the Si anode when plasticity is suppressed.[9]

We have carried out such calculations for several different C-rates. Figs. 9(c) and (d), respectively, show the total dissipation per cycle as a function of C-rate, and the maximum capacity (SOC at $V = 0.01$ V) as a function of C-rate. Clearly, the simulations without plasticity produce significantly different results than those with plasticity.

For an informative movie which compares simulations with and without plasticity, please see the supplementary movie "S3_HollowTube_PlasticComp.mp4". This movie shows the time-dependent contour plots of the normalized concentration $\bar{c}$ and the equivalent plastic strain $\bar{\epsilon}^p$ on the deformed geometry of the a-Si nanotube anode. It also shows the variation of the voltage V versus SOC during the simulation.

5 Concluding remarks

We have formulated and numerically implemented a fully-coupled diffusion-deformation theory, which accounts for transient diffusion of lithium and accompanying large elastic-plastic deformations of a-Si. The material parameters in the theory have been calibrated to results from experiments reported in the literature. We have applied our numerical simulation capability to model galvanostatic charging of hollow a-Si

[9] There are two possible dissipation mechanism in the electrode, one due to plastic deformation, and one due to gradients in the chemical potential (c.f. eq. (8.11) in Anand, 2012). In our simulations, due to the nano-metric size of the anodes considered, the gradients of the chemical potential are very small and consequently the dissipation due to gradients in the chemical potential is very small.

nanotubes whose exterior walls have been oxidized to prevent outward expansion (Wu et al., 2012). We have shown that the results from our numerical simulations are in good agreement with the experimentally-measured voltage versus SOC behavior at various charging rates (C-rates). Through our simulations, we have identified two major effects of plasticity on the performance of a-Si-based anodes:

- First, plasticity enables lithiation of the anode to a higher SOC for a given voltage cut-off. This is because plastic flow reduces the stresses generated in the material, and thus reduces the potential required to lithiate the material.
- Second, plastic deformation accounts for a significant amount of the energy dissipated during the cycling of the anode at low C-rates. For the particular geometry of the anode considered in this paper, plasticity accounts for over 30% of the total dissipation per cycle at a low C-rate of 1/10.

Hence, plasticity can have either a beneficial effect — that is, a higher SOC for a given voltage cut-off, or a detrimental effect — that is, significant energy dissipation at low C-rates, on the electrochemical performance of a-Si-based anodes.

The design of a-Si-based anodes for optimal performance is non-trivial. The fully-coupled diffusion-deformation theory and simulation capability reported in this paper should be useful in developing a detailed understanding of the electro-chemo-mechanical operation of a-Si-based anodes, and optimizing their design for future applications. Furthermore, the favorable comparison between the predictions from our continuum theory and the experimental results shown in this work, demonstrates the applicability and importance of continuum-level models in making meaningful predictions of the electrochemical response of a-Si based nanostructured anodes.

Finally, the theory and numerical simulation tools developed in this work will help one to formulate models at the porous-electrode-scale, where one must consider the interactions between anode particles and binder and between anode particles themselves. Using the foundations developed here, such a (non-trivial) extension of this work will allow one to study how the stresses generated within an anode particle affects its interaction with other particles, as well as study how the stresses generated in the microstructure might affect loss of conductivity due to failure of the anode-particle/binder interfaces.

Acknowledgements

The authors gratefully acknowledge the support provided by NSF, CMMI Award No. 1063626.

A Appendix. Details of modeling interfacial reaction kinetics.

Electrochemical potential: The **electrochemical potential** of the ith charged species in a chemical reaction is defined as

$$\tilde{\mu}_i \stackrel{\text{def}}{=} \mu_i + z_i F \phi_I, \tag{A.1}$$

where μ_i is its **chemical potential**, z_i is its valence, F is Faraday's constant,[10] and ϕ_I is the electric potential in phase I in which the charged species is found.[11]

Consider an electrode containing some Li submerged in a bath of an electrolyte containing Li^+ ions. We make the following assumptions regarding this system:

- The electrode material is considered insoluble in the electrolyte.
- We assume that within the electrode there are more than enough electrons to combine with the Li ions, so that lithium in the electrode exists as a *neutral species*.
- We consider the electrical conductivity of the electrode to be large, and the diffusion of Li^+ through the electrolyte to be fast.

[10] The Faraday constant is the magnitude of electric charge per mole of electrons. It has a value $9.64853399(24) \times 10^4$ C mol^{-1}.

[11] Henceforth we distinguish the electrochemical potential with an overset tilde, $\tilde{\mu}$, while the chemical potential, μ, will not have an overset tilde.

- We denote the electric potential in the electrode by ϕ^{e}, and the electric potential in the electrolyte by ϕ. Further, we assume that both of these electric potentials are constant, and variations in the electric potential occur only at the electrode/electrolyte interface.

Consider now the following electrochemical reaction at the surface of the electrode,

$$\mathrm{Li}^{(\text{electrode surf.})} \rightleftarrows \mathrm{Li}^{+(\text{electrolyte})} + \mathrm{e}^{-(\text{electrode surf.})}, \tag{A.2}$$

and let

$$\tilde{\mu}_{\mathrm{Li}}^{(\text{electrode surf.})}, \quad \tilde{\mu}_{\mathrm{Li}^+}^{(\text{electrolyte})}, \quad \text{and} \quad \tilde{\mu}_{\mathrm{e}^-}^{(\text{electrode surf.})}, \tag{A.3}$$

respectively, denote the the electrochemical potentials of the Li atoms on the surface of the electrode, Li ions in the electrolyte, and the electrons on the surface of the electrode.

Remark. Henceforth, for brevity, we will omit the superscripts used in (A.2) and (A.3) to denote the location of each species. Thus, for the ensuing discussion, the neutral Li as well as the electrons should always be considered as being on the the surface of the electrode, while the Li^+ ions should always be considered as being in the electrolyte. Hence, the subscript denoting the species type is also an indicator of its location. □

Let the difference between the electrochemical potentials of the reactant and products in (A.2) divided by Faraday's constant be denoted by

$$\eta \stackrel{\text{def}}{=} \frac{1}{F}\Big(\tilde{\mu}_{\mathrm{Li}} - (\tilde{\mu}_{\mathrm{Li}^+} + \tilde{\mu}_{\mathrm{e}^-})\Big). \tag{A.4}$$

This represents a "driving force" for the chemical reaction (A.2) in the sense that:

- If $\eta > 0$, then lithium is favored to be expelled form the electrode into the electrolyte — Li is oxidized to form Li^+.
- If $\eta < 0$, then lithium is favored to be intercalated form the electrolyte into the electrode — Li^+ is reduced to form Li.
- And, the condition $\eta = 0$ represents the condition for **equilibrium** of the reaction in equation (A.2).

The electrochemical potentials in (A.4) may be further expressed in terms of their chemical potentials and electric potentials as

$$\begin{aligned} \tilde{\mu}_{\mathrm{Li}} &= \mu_{\mathrm{Li}}, \\ \tilde{\mu}_{\mathrm{Li}^+} &= \mu_{\mathrm{Li}^+} + F\phi, \\ \tilde{\mu}_{\mathrm{e}^-} &= \mu_{\mathrm{e}^-} - F\phi^{\mathrm{e}}, \end{aligned} \tag{A.5}$$

where in writing (A.5) we have made use of the fact that Li atoms in the electrode are a *neutral species*, that the Li ions are positively charged (valance of +1), and that the electrons are negatively charged (valance of −1). Further note that the electric potential acting on the Li ions is that of the electrolyte, ϕ, and the electric potential acting on the electrons is that of the electrode, ϕ^{e}.

Next, consistent with our earlier assumptions, we assume further that the activities of the Li^+ ions in the electrolyte and the electrons e^- in the electrode have a value of unity[12] — that is the electrolyte and the electrode may be treated as infinite reservoirs which supply Li^+ ions and electrons e^- to the chemical reaction at the surface of the electrode particle. Then, the electrochemical potentials (A.5) may be written as

$$\begin{aligned} \tilde{\mu}_{\mathrm{Li}} &= \mu^0_{\mathrm{Li}} + \hat{\mu}_{\mathrm{Li}}(\bar{c}, \mathbf{M}^e, \vartheta), \\ \tilde{\mu}_{\mathrm{Li}^+} &= \mu^0_{\mathrm{Li}^+} + F\phi, \\ \tilde{\mu}_{\mathrm{e}^-} &= \mu^0_{\mathrm{e}^-} - F\phi^{\mathrm{e}}, \end{aligned} \tag{A.6}$$

[12]The chemical potential of a species is usually written as

$$\mu_i = \mu_i^0 + R\vartheta \ln(a_i),$$

where a_i represents the *activity* of the species, and μ_i^0 represents the reference value when $a_i = 1$.

where the reference potentials $\mu^0_{\rm Li}$, $\mu^0_{\rm Li^+}$ and $\mu^0_{\rm e^-}$ are constants, and where we have recalled that the chemical potential of the Li at the surface of the electrode is a function of the concentration, the Mandel stress, and the temperature, (c.f. eq. 2.7). Using (A.6) we may write the quantity η defined (A.4) as

$$\eta = \frac{\hat{\mu}_{\rm Li}(\bar{c}, \mathbf{M}^e, \vartheta)}{F} - \frac{(\mu^0_{\rm Li^+} + \mu^0_{\rm e^-} - \mu^0_{\rm Li})}{F} + \Delta\phi, \tag{A.7}$$

where

$$\Delta\phi \stackrel{\rm def}{=} (\phi^{\rm e} - \phi), \tag{A.8}$$

represents the *voltage drop* across the electrode/electroyte interface.

Equilibrium: At equilibrium $\eta = 0$. Thus, using (A.7), we may define an *equilibrium interfacial voltage* as

$$\Delta\phi_{\rm eq} = V_0^* - \frac{\hat{\mu}_{\rm Li}(\bar{c}, \mathbf{M}^e, \vartheta)}{F}, \tag{A.9}$$

where

$$V_0^* \stackrel{\rm def}{=} \frac{(\mu^0_{\rm Li^+} + \mu^0_{\rm e^-} - \mu^0_{\rm Li})}{F} \equiv \text{constant}. \tag{A.10}$$

In the absence of stresses, (A.9) represents the standard Nernst equation for the system under consideration.

Using (A.9), we may rewrite (A.7) as

$$\eta = \Delta\phi - \Delta\phi_{\rm eq}. \tag{A.11}$$

The quantity η is commonly referred to as the **overpotential**, since — as is clear from (A.11) — it represents the electric potential above (or below) an equilibrium value required to drive the chemical reaction.

Deviation from equilibrium: When the overpotential $\eta \neq 0$, the chemical reaction (A.2) takes place, and there is a resulting current I. The current I *per unit area* is a function of the overpotential η, and is widely taken to be given by the phenomenological Butler-Volmer equation (cf., e.g., Newman and Thomas-Alyea, 2012; Bazant, 2013),

$$I = I_0 \left(\exp\left(-\alpha \frac{F\eta}{R\vartheta} \right) - \exp\left((1-\alpha) \frac{F\eta}{R\vartheta} \right) \right). \tag{A.12}$$

Here, I_0 is a concentration-dependent *exchange current*, given by

$$I_0 = F k_0 (1-\bar{c})^{\alpha} \bar{c}^{(1-\alpha)}, \tag{A.13}$$

$0 < \alpha < 1$ is a symmetry factor which biases the reaction, and k_0 is a rate constant which is typically determined experimentally. In our simulations we assume $\alpha = 0.5$, in which case (A.12) may be inverted to yield

$$\eta = 2\frac{R\vartheta}{F} \sinh^{-1}\left(-\frac{1}{2}\frac{I}{I_0} \right), \quad \text{with} \quad I_0 = F k_0 (1-\bar{c})^{1/2} (\bar{c})^{1/2}. \tag{A.14}$$

Equilibrium potential. Cell voltage: Let

$$\Delta\phi_{\rm cnt} \stackrel{\rm def}{=} \phi^{\rm cnt} - \phi,$$

define the voltage drop at the counter-electrode/electrolyte interface in the half-cell, where $\phi^{\rm cnt}$ is the electric potential of the counter-electrode which is a constant. Then, we define an **equilibrium potential** for the half-cell through

$$U \stackrel{\rm def}{=} \Delta\phi_{\rm eq} - \Delta\phi_{\rm cnt}. \tag{A.15}$$

Then, using (A.15) and (A.9), we obtain that

$$U = V_0 - \frac{\hat{\mu}_{\rm Li}(\bar{c}, \mathbf{M}^e, \vartheta)}{F}, \qquad \text{where} \qquad V_0 \stackrel{\rm def}{=} V_0^* - \Delta\phi_{\rm cnt} \equiv \text{constant}. \tag{A.16}$$

Thus, the parameter V_0 depends on the counter-electrode used. It is a Li foil in all the experiments considered in this paper.

Finally, the **cell voltage** is defined as the voltage drop between the electrode and the counter electrode

$$\begin{aligned} V &\stackrel{\text{def}}{=} \phi^e - \phi^{\text{cnt}} \\ &= (\phi^{\text{e}} - \phi) - (\phi^{\text{cnt}} - \phi) = \Delta\phi - \Delta\phi_{\text{cnt}}, \end{aligned} \tag{A.17}$$

where in writting (A.17) we have made use of the assumption that the electrolyte electric potential ϕ is constant through the electrolyte. Using (A.11), (A.14), and (A.16) the cell voltage may be written as

$$\begin{aligned} V &= U + \eta \\ &= V_0 - \frac{\hat{\mu}_{\text{Li}}(\bar{c}, \mathbf{M}^e, \vartheta)}{F} + 2\frac{R\vartheta}{F}\sinh^{-1}\left(-\frac{1}{2}\frac{I}{I_0}\right). \end{aligned} \tag{A.18}$$

Flux boundary condition: As discussed in $(2.20)_2$, at a point on the surface of the deformed body we may prescribe a flux boundary condition, $\mathbf{j}\cdot\mathbf{n} = \breve{j}$. The prescribed flux $\breve{j}$ is related to an applied current I per unit area at that point by

$$\breve{j} = -I/F. \tag{A.19}$$

Remark. When a battery is cycled under constant current conditions, that is galvanostatic conditions, it is the *total* current

$$I_{\text{total}} = \int_{\partial\mathcal{B}_t} I\, da,$$

which is constant across the electrode. In a finite-element simulation of an arbitrary shaped-electrode which has been discretized to have m elements on the exterior boundary of the body, one must prescribe an *integral* constraint of the form

$$I_{\text{total}} = \sum_{k=1}^{m}\int_{\partial\mathcal{B}_t^e} I_k\, da = \sum_{k=1}^{m}\int_{\partial\mathcal{B}_t^e} -F\,\breve{j}_k\, da$$

where $\breve{j}_k$ represents the flux to be prescribed on the desired surface of the k-th element. However, in the simulations considered in this paper the diffusion is essentially one-dimensional in nature, there is a single element on the surface of our simulation domains, and the simple eq. (A.19) applies. □

References

Abaqus/Standard, 2010. SIMULIA, Providence, RI.

Anand, L., 2012. A Cahn-Hilliard-type theory for species diffusion coupled with large elastic-plastic deformations. Journal of the Mechanics and Physics of Solids 12, 1983-2002.

Newman, J., Thomas-Alyea, E., 2012. Electrochemical systems. John Wiley & Sons.

Berla, L.A., Lee, S.W., Cui, Y., Nix, W.D. (2014). Robustness of amorphous silicon during the initial lithiation/delithiation cycle. Journal of Power Sources, 258, 2530259.

Bower, A.F., Guduru, P.R., Sethuraman, V.A., 2011. A finite strain model of stress, diffusion, plastic flow, and electrochemical reactions in a lithium-ion half-cell. Journal of the Mechanics and Physics of Solids 59, 804–828.

Bazant, M.Z., 2013. Theory of chemical kinetics and charge transfer based on nonequilibrium thermodynamics. Accounts of chemical research 46.5, 1144-1160.

Bucci, G., Nadimpalli, S.P., Sethuraman, V.A., Bower, A.F., Guduru, P.R., 2014. Measurement and modeling of the mechanical and electrochemical response of amorphous Si thin film electrodes during cyclic lithiation. Journal of the Mechanics and Physics of Solids, 62, 276-294.

Chester, S.A., Di Leo, C.V., Anand, L., 2014. A finite element implementation of a coupled diffusion-deformation theory for elastomeric gels. International Journal of Solids and Structures 52, 1-18.

Di Leo, C.V., Rejovitzky, E., Anand, L., 2014. A Cahn-Hilliard-type phase-field theory for species diffusion coupled with large elastic deformations: Application to phase-segragating Li-ion electrode materials. J. Mech. Phys. Solids, 70, 1-29.

Ding, N., Xu, J., Yao, Y.X., Wegner, G., Fang, X., Chen, C.H., Lieberwirth, I., 2009. Determination of the diffusion coefficient of lithium ions in nano-Si. Solid State Ionics, 180(2), 222-225.

Gurtin, M.E., Fried, E., Anand, L., 2010. The Mechanics and Thermodynamics of Continua. Cambridge University Press, Cambridge.

He, Y., Xu, X., Wang, Y., Li, H., Huang, X., 2011. Alumina-Coated Patterned Amorphous Silicon as the Anode for a Lithium-Ion Battery with High Coulombic Efficiency. Adv. Mater, 23, 4938 - 4941.

Li, H., Huang, X., Chen, L., Wu, Z., Liang, Y., 1999. A High Capacity Nano-Si Composite Anode Material for Lithium Rechargeable Batteries. Electrochemical and Solid-State Letters 2(11), 547-549.

Liu, X.H., Zhong, L., Huang, S., Mao, S.X., Zhu, T., Huang, J.Y., 2012. Size-dependent fracture of silicon nanoparticles during lithiation. Acs Nano, 6(2), 1522 - 1531.

McDowell, M.T. Ryu, I., Lee, S.W., Wang, C., Nix, W.D., Cui, Y. 2012. Studying the kinetics of crystalline silicon nanoparticle lithiation with in situ transmission electron microscopy. Adv. Mater, 24, 6034 - 6041.

McDowell, M.T., Lee, S.W., Harris, J.T., Korgel, B.A., Wang, C.. Nix, W.D., Cui, Y., 2013. In situ TEM of two-phase lithiation of amorphous silicon nanospheres. Nano Letters 13, 758-764.

Mohr, P.J., Taylor, B.N., Newell, D.B., 2008. Codata recommended values of the fundamental physical constant. Rev. Mod. Phys. 90, 633730.

Obrovac, M.N., Krause, L.J., 2007. Reversible cycling of crystalline silicon powder. Journal of the Electrochemical Society 154, A103–A108.

Pharr, M., Suo, Z., Vlassak, J.J., 2014. Variation of stress with charging rate due to strain-rate sensitivity of silicon electrodes of Li-ion batteries. Journal of Power Sources.

Pinson, M.B., Bazant, M.Z., 2013. Theory of SEI formation in rechargeable batteries: capacity fade, accelerated aging and lifetime prediction. Journal of The Electrochemical Society, 160(2), A243-A250.

Rejovitzky, E., Di Leo, C.V., Anand, L., 2014. A theory and simulation capability for growth of a solid electrolyte interphase layer at an anode particle in a Li-ion battery. Journal of the Mechanics and Physics of Solids 78, 210-230.

Ryu, I., Choi, J.W., Cui, Y., Nix, W.D., 2011. Size-dependent fracture of Si nanowire battery anodes. Journal of the Mechanics and Physics of Solids, 59, 1717-1730.

Scrosati, B., and Garche, J., 2010. Lithium batteries; status, prospects and future. Journal of Power Sources 195, 2419–2430.

Sethuraman, V.A., Srinivasan, V., Bower, A.F., Guduru, P.R., 2010. In Situ Measurements of Stress-Potential Coupling in Lithiated Silicon. J. Electrochem. Soc., 11, A1253 — A1261.

Sethuraman, V. A., Chon, M. J., Shimshak, M., Van Winkle, N., Guduru, P. R, (2012). *In situ* measurement of biaxial modulus of Si anode for Li-ion batteries. Electrochemistry Communications, 12(11), 1614-1617.

Smith, A.J., Burns, J.C., Zhao, X., Xiong, D., Dahn, J.R., 2011. A high precision coulometry study of the SEI growth in Li/graphite cells. Journal of The Electrochemical Society, 158(5), A447-A452.

Stoney, G.G., 1909. The tension of metallic films deposited by electrolysis. Proceeding of the Royal Society A 82, 172-175.

Tarascon, J., Armand, M., 2001. Issues and challenges facing rechargeable batteries. Nature 414, 359-367.

Wang, J.W., Yu, H., Feifei, F., Liu, X.H., Xia, S., Liu, Y., Harris, C.T., Li, H., Huang, J.Y., Mao, S.X., Zhu, T., 2013. Two-phase electrochemical lithiation in amorphous silicon. Nano Letters 13, 709-715.

Wu, H., Chan, G., Choi, J. W., Yao, Y., McDowell, M. T., Lee, S. W., Jackson, A., Yang, Y., Hu, L., and Cui, Y. (2012). Stable cycling of double-walled silicon nanotube battery anodes through solid-electrolyte interphase control. Nature nanotechnology, 7(5), 310-315.

Zhang, Y., Li, Y., Wang, Z., Zhao, K., 2014. Lithiation of SiO_2 in Li-Ion Batteries: In Situ Transmission Electron Microscopy Experiments and Theoretical Studies. Nano letters 14(12), 7161-7170.

Zhao, K., Pharr, M., Cai, S.,Vlassak, J.J., Suo, Z., 2011. Large plastic deformation in high-capacity lithium-ion batteries caused by charge and discharge. Journal of American Ceramic Society 94, S226–S235.

Zhao, K., Pharr, M., Hartle, L., Vlassak, J.J., Suo, Z., 2012. Fracture and debonding in lithium-ion batteries with electrodes of hollow core-shell nanostructures. Journal of Power Sources 218, 6-14.

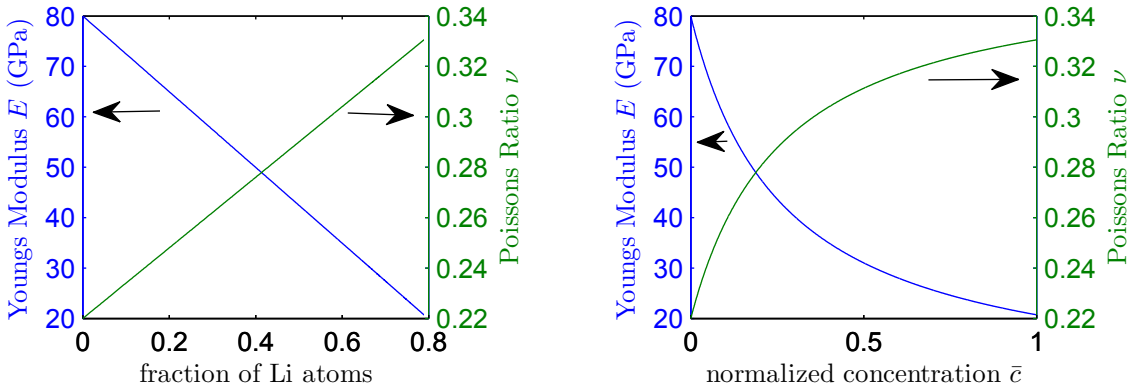

Figure 1: Variation of the elastic constants in Li_xSi as a function of (a) the fraction of Li atoms (number of Li atoms/total number of atoms), and (b) as a function of the normalized Li concentration $\bar{c}$.

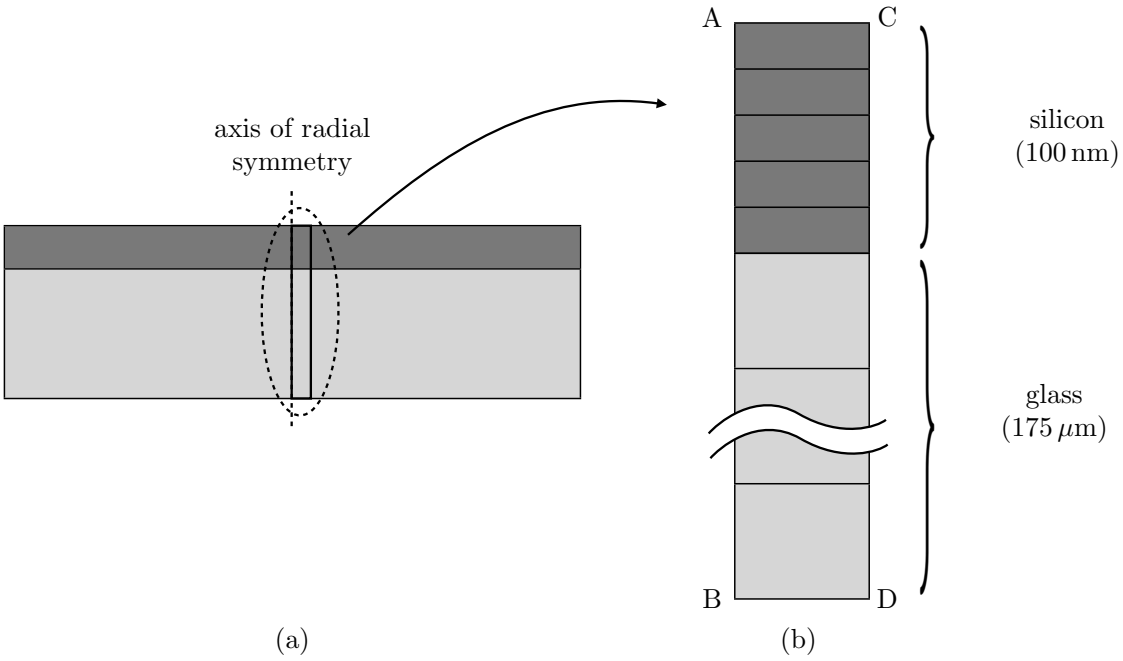

Figure 2: (a) Plate geometry showing simulation domain at the axis of radial symmetry, and (b) schematic of the single-column finite-element mesh used in the substrate curvature simulations.

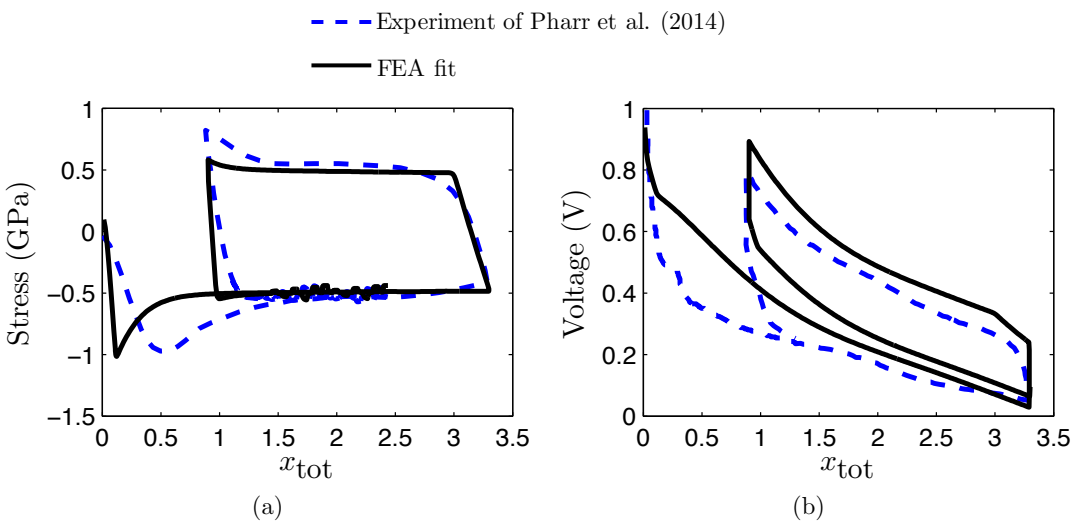

Figure 3: Fit of our substrate curvature simulation to the experiments of Pharr et al. (2014) showing (a) the nominal stress in the Si film, and (b) the voltage, both as functions of the total lithium content.

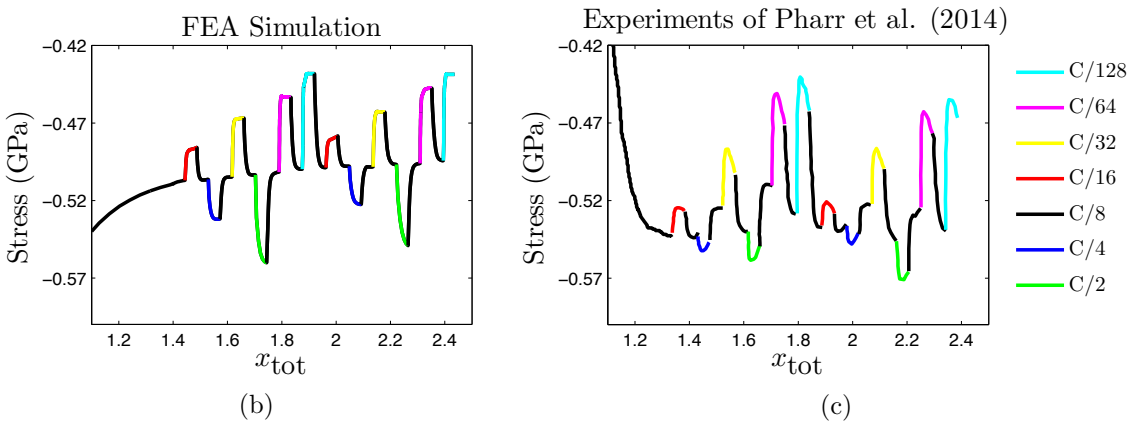

Figure 4: Nominal stress jumps produced by varying the C-rate from (a) our finite-element simulation, and (b) the experiments of Pharr et al. (2014).

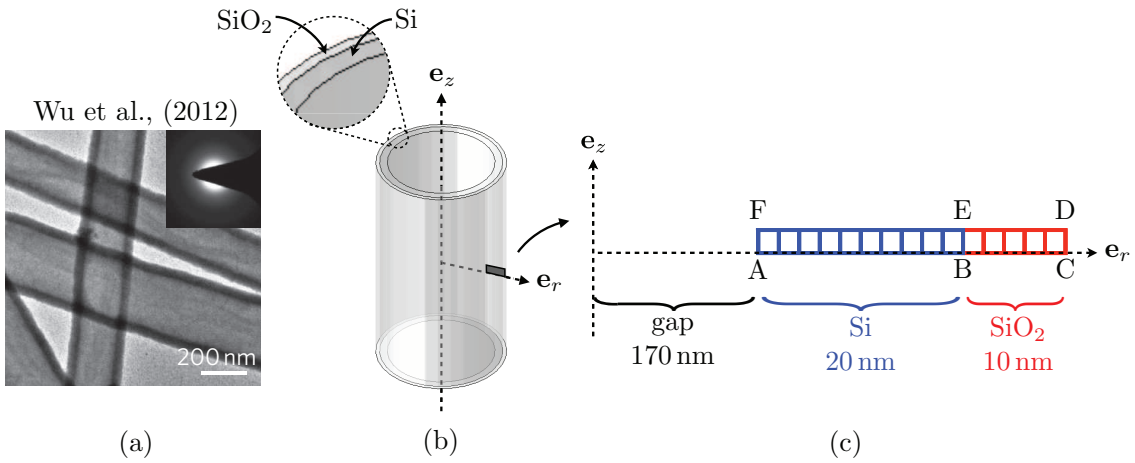

Figure 5: Modeling hollow double-walled nanotubes. (a) Shows a TEM of the experimentally-realized nanotubes reproduced from Wu et al. (2012). (b) Shows a representative hollow double-walled nanotube where, consistent with our assumptions of axisymmetry and radial diffusion, we take a sliver of the tube on the $\mathbf{e}_z$-$\mathbf{e}_r$ plane as our simulation domain. (c) Shows a schematic of the simulation domain (not to scale) and a representative finite-element mesh.

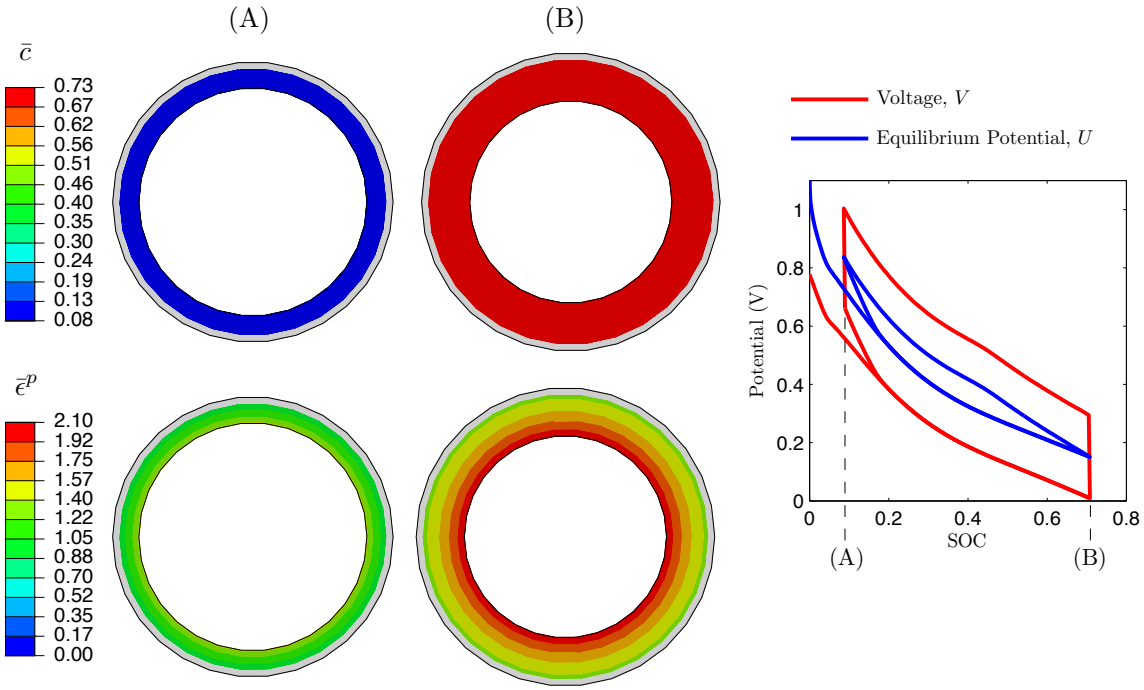

Figure 6: Simulation of a hollow double-walled nanotube anode cycled at a C-rate of 1 between voltage limits of 0.01 and 1 V for 3 half-cycles. Contours of normalized concentration $\bar{c}$ (top) and equivalent plastic strain $\bar{\epsilon}^p$ (bottom), in the a-Si anode, at (A) the start, and (B) the end of the last half-cycle. On the right we plot the voltage V, and equilibrium potential U, as functions of SOC, for the same simulation.

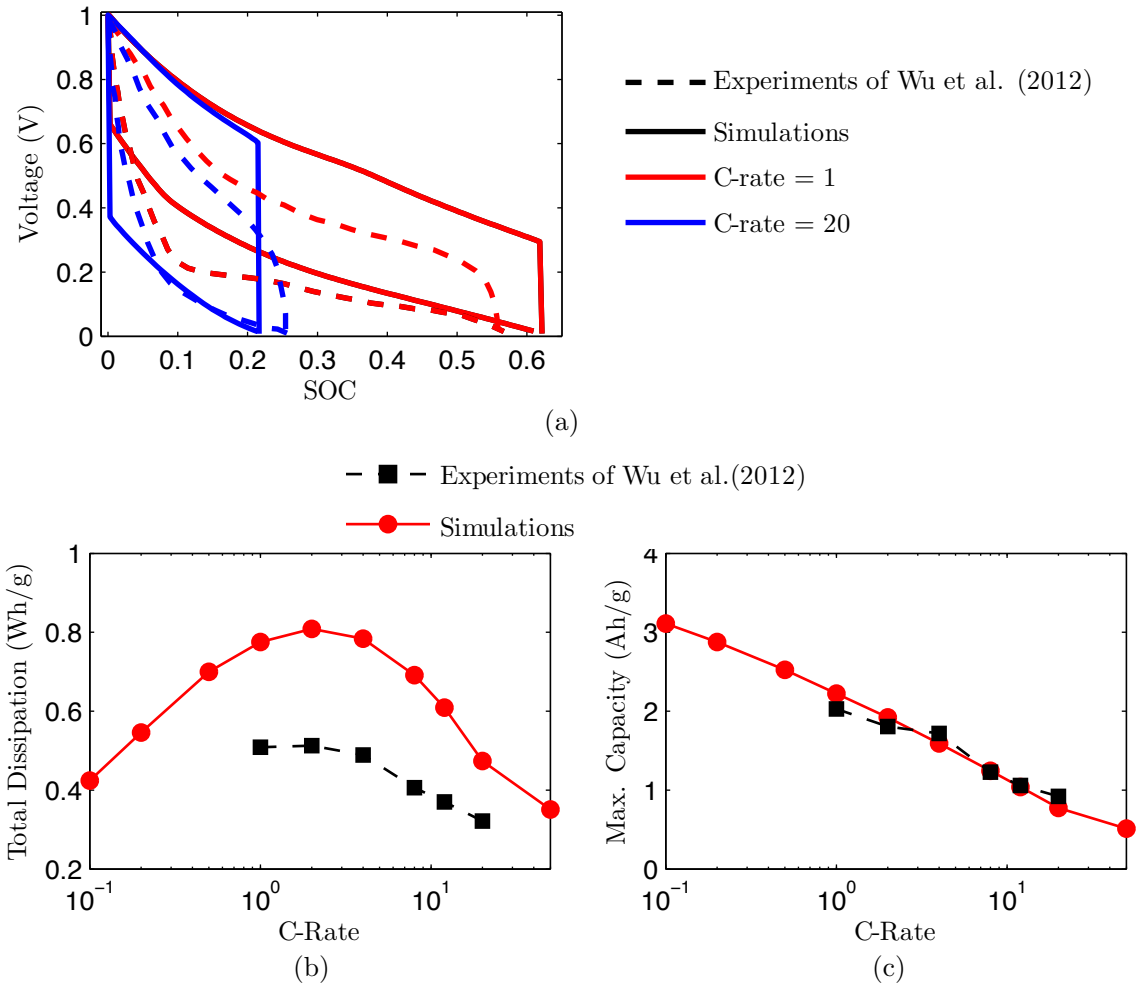

Figure 7: Comparison between simulated hollow double-walled nanotubes and the experiments of Wu et al. (2012). (a) Voltage versus SOC at C-rates of 1 and 20, (b) total dissipation over one full cycle as a function of C-rate, and (c) maximum capacity (i.e. SOC at cutoff of $V = 0.01\,\mathrm{V}$) as a function of C-rate.

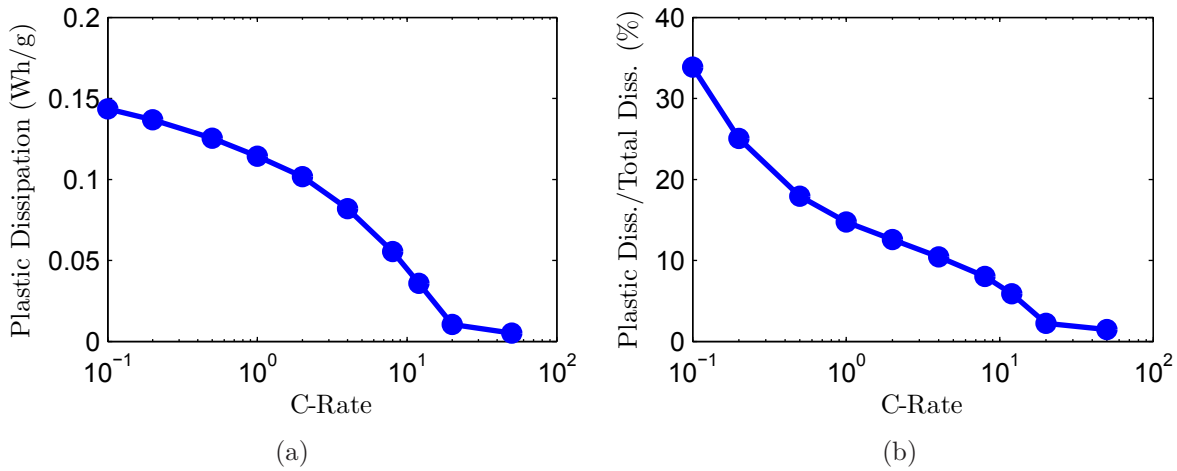

Figure 8: Simulations of hollow double-walled nanotubes. (a) Plastic dissipation over one full cycle as a function of C-rate. (b) Plastic dissipation normalized by total dissipation, in percent, as a function of C-rate. Note the logarithmic x-axis.

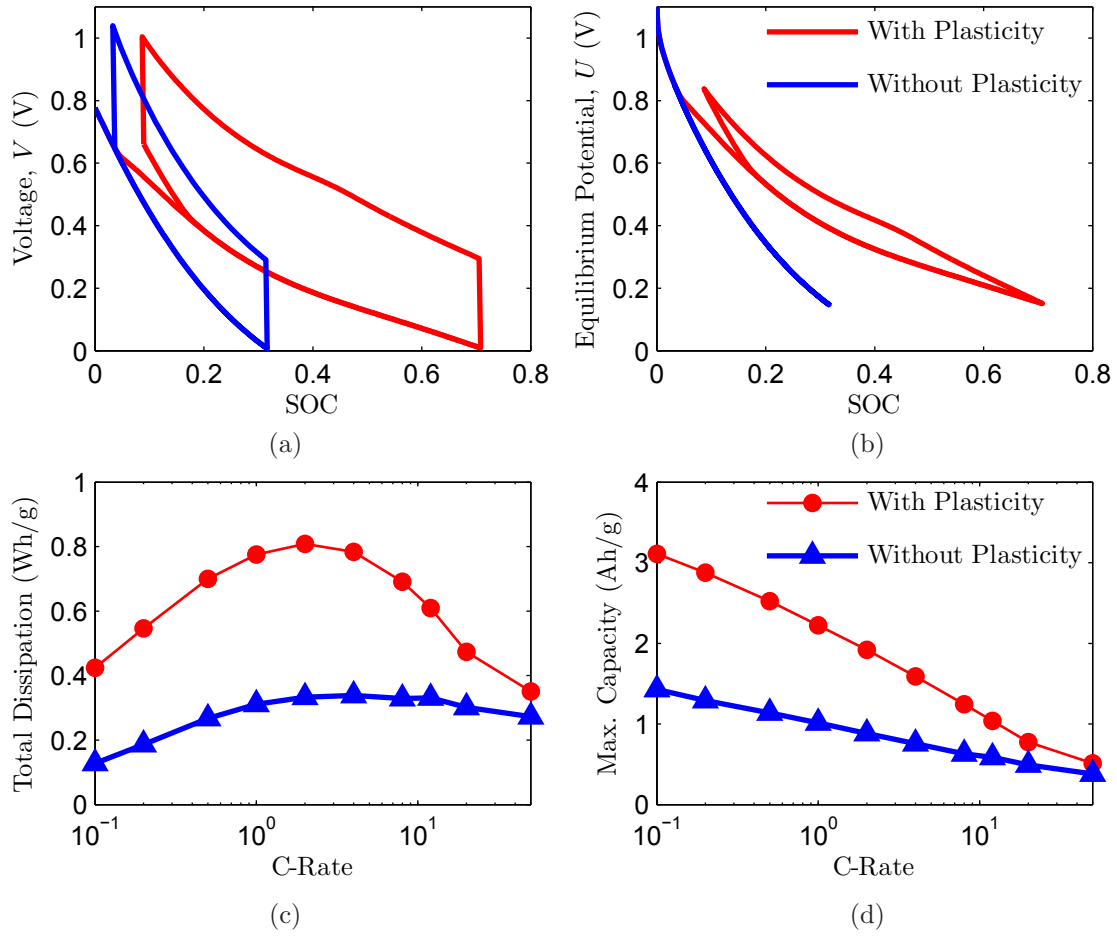

Figure 9: Simulations of hollow double-walled nanotubes with and without plasticity. (a) Voltage versus SOC, (b) equilibrium potential versus SOC, (c) total dissipation over one cycle versus C-rate, and (d) maximum capacity (i.e. SOC at cutoff of $V = 0.01$ V) versus C-rate. Note the logarithmic x-axis.